

Linear and nonlinear paraconductivity in bilayer multiphase superconductors

Tsugumi Matsumoto,* Youichi Yanase, and Akito Daido

Department of Physics, Graduate School of Science, Kyoto University, Kyoto 606-8502, Japan

(Dated: May 24, 2024)

Thin-film multiphase superconductors are attracting much attention, and it is an important issue to propose how to detect them in experiments. In this work, we study the linear and nonlinear paraconductivity of a bilayer model with staggered Rashba-type spin-orbit coupling with and without the potential gradient. This model shows the Bardeen-Cooper-Schrieffer phase, pair-density-wave phase, and Fulde-Ferrell-Larkin-Ovchinnikov (FFLO) phase, and we focus on how their properties are encoded to the charge transport. We show that the linear paraconductivity has a peak associated with the phase transitions between different superconducting states due to the degeneracy of the transition temperatures as well as the paramagnetic depairing effect. We also show that the FFLO superconducting state shows a sizable nonlinear paraconductivity once the degeneracy of Cooper pairs is lifted by applying the potential gradient. Observation of the peaked linear and nonlinear paraconductivity can be used as a probe of multiphase superconductivity.

I. INTRODUCTION

Multiphase superconductors, which have several superconducting states in a phase diagram, are platforms of many attractive and characteristic features and are candidates for exotic superconducting states such as odd-parity, spin-triplet [1], and topological superconductivity [2–5]. For instance, CeRh₂As₂ is considered to have two superconducting phases at ambient pressure and one of the superconducting phases is supposed to realize an odd-parity superconducting state [6–21]. UTe₂ is known to realize various superconducting states by changing the pressure and magnetic field and considered to be a candidate of spin-triplet superconductors and topological superconductors [14, 22–45]. These materials have been investigated intensively, and the superconducting multiphases have been identified mainly by using thermodynamic and magnetic measurements.

In addition to the bulk multiphase superconductors, atomically thin film superconductors have emerged as a new and important platform for multiphase superconductors after the technical development of thin-film fabrication. For instance, CeCoIn₅ thin films and superlattices [46] are considered to be candidates of multiphase superconductors which may have not only the Bardeen-Cooper-Schrieffer (BCS) state but also the pair-density wave (PDW) state and/or Fulde-Ferrell-Larkin-Ovchinnikov (FFLO) state [47–49]. Although FFLO superconductivity was proposed a long time ago [50, 51], its presence is still elusive and new probes are awaited. Moreover, TaS₂ [52–57] intercalated with chiral molecules has the potential to realize the PDW state [58]. The PDW state is an odd-parity superconducting state, which is rare in nature, and therefore, has attracted much attention. Finite-momentum superconductivity beyond the conventional FFLO state has also been reported in multilayer NbSe₂ [59].

Generally speaking, available experimental probes are limited for thin-film superconductors compared with bulk superconductors, since thermodynamic measurements are difficult to be performed. In this regard, the electric measurements, including reciprocal and nonreciprocal charge transport [60–63], may offer suitable probes of thin-film multiphase superconductors. In this study, we focus on the linear and nonlinear paraconductivity of bilayer systems with a staggered Rashba-type spin-orbit coupling [64] as a simple example of multiphase superconductors [64–68]. The paraconductivity refers to the excess conductivity by the thermally-fluctuating Cooper pairs at temperature slightly larger than the mean-field transition temperature [62, 69–75]. This model has the BCS and PDW phases in the perpendicular magnetic fields [64], while has the BCS and FFLO phases in the in-plane magnetic field [76], allowing us to study the two representative superconducting multiphases. While the original model preserves the global inversion symmetry, we can also study the nonlinear paraconductivity by applying the potential gradient and breaking the inversion symmetry, when the magnetic field has an in-plane component. We show that the degeneracy of the superconducting states in multiphase and/or finite-momentum superconductors give rise to characteristic features in linear and nonlinear paraconductivity, and thereby argue that they can be used as a probe of the exotic superconducting states.

This paper is organized as follows. In Sec. II, we introduce the model Hamiltonian and the methods including the general formulas to calculate the paraconductivity. In Sec. III, we consider the system in the perpendicular magnetic field. First, we consider the system with inversion symmetry. We show the superconducting phase diagram which includes the first- and second-order superconducting transition lines. We discuss the linear paraconductivity with particular emphasis on its behavior near the first-order phase transition point between the BCS and PDW phases. Then, we apply a potential gradient to break inversion symmetry and discuss its impact on the features of the linear paraconductivity.

* matsumoto.tsugumi.78w@st.kyoto-u.ac.jp

In Sec. IV, we consider the system in the in-plane magnetic field with the BCS and FFLO phases. We show the linear and nonlinear paraconductivity with and without the potential gradient and discuss their features from the perspective of the degeneracy of superconducting states and/or Cooper pair momenta. We summarize the results in Sec. V.

II. SETUP AND FORMULATION

In this section, we introduce the model and the general formulas to calculate the linear and nonlinear paraconductivity.

A. Bilayer model with staggered Rashba spin-orbit coupling

We consider a bilayer model with staggered Rashba-type spin-orbit coupling [64],

$$\hat{H} = \hat{H}_{\parallel} + \hat{H}_{\perp} + \hat{H}_{\text{int}} + \hat{H}_{\text{Rashba}} + \hat{H}_{\text{Zeeman}}, \quad (1)$$

$$\hat{H}_{\parallel} = \sum_{\mathbf{k}, s, m} \xi(\mathbf{k}) c_{\mathbf{k}sm}^{\dagger} c_{\mathbf{k}sm}, \quad (2)$$

$$\hat{H}_{\perp} = t_{\perp} \sum_{\mathbf{k}, s, \langle m, m' \rangle} c_{\mathbf{k}sm}^{\dagger} c_{\mathbf{k}sm'}, \quad (3)$$

$$\begin{aligned} \hat{H}_{\text{int}} = \sum_{\mathbf{k}, \mathbf{k}', \mathbf{q}, m} U(\mathbf{k}, \mathbf{k}', \mathbf{q}) c_{\mathbf{k}+\mathbf{q}/2\uparrow m}^{\dagger} c_{-\mathbf{k}+\mathbf{q}/2\downarrow m}^{\dagger} \\ \times c_{-\mathbf{k}'+\mathbf{q}/2\downarrow m} c_{\mathbf{k}'+\mathbf{q}/2\uparrow m}, \end{aligned} \quad (4)$$

$$\hat{H}_{\text{Rashba}} = \sum_{\mathbf{k}, s, s', m} \alpha_m \mathbf{g}(\mathbf{k}) \cdot \boldsymbol{\sigma}_{ss'} c_{\mathbf{k}sm}^{\dagger} c_{\mathbf{k}s'm}, \quad (5)$$

$$\hat{H}_{\text{Zeeman}} = - \sum_{\mathbf{k}, s, s', m} \mu_B \mathbf{H} \cdot \boldsymbol{\sigma}_{ss'} c_{\mathbf{k}sm}^{\dagger} c_{\mathbf{k}s'm}, \quad (6)$$

where $m = 1, 2$ is the layer index and $s = \uparrow, \downarrow$ is the spin index. Here, we define $\langle m, m' \rangle$ to be summation for nearest-neighbor layers, namely, $(m, m') = (1, 2)$ and $(2, 1)$. $\xi(\mathbf{k}) = -2t(\cos k_x + \cos k_y) - \mu$ represents intralayer hopping energy, and $\mathbf{g}(\mathbf{k}) = (-\sin k_y, \sin k_x, 0)$ represents the Rashba-type spin-orbit coupling. The magnetic field $\mathbf{H} = (H_x, H_y, H_z)$ is applied either in the out-of-plane ($H_x = H_y = 0$) or in the in-plane ($H_z = H_x = 0$) directions. Here we set α_m to be $(\alpha_1, \alpha_2) = (+\alpha, -\alpha)$, and thus the system has the global inversion symmetry. We assume isotropic s-wave superconductivity and apply the mean-field approximation to the Hamiltonian. For simplicity, we assume $U(\mathbf{k}, \mathbf{k}', \mathbf{q}) = -U$ with the onsite attractive interaction U and introduce the order parameters as

$$\Delta_m(\mathbf{q}) = -U \sum_{\mathbf{k}} \langle c_{-\mathbf{k}+\mathbf{q}/2\downarrow m} c_{\mathbf{k}+\mathbf{q}/2\uparrow m} \rangle, \quad (7)$$

which describes the spin-singlet s-wave Cooper pairs in each layer $m = 1, 2$. In this study, we set parameters to $(t, t_{\perp}, \mu, U) = (1.0, 0.1, 2.0, 1.7)$ and adopt the unit $\mu_B = k_B = 1$. It is known that the superconducting phase diagram depends on the value of α , and the superconducting multiphase including the BCS and PDW phases appears in the perpendicular magnetic field when α/t_{\perp} takes a sufficiently large value [64]. To study the superconducting multiphase, we set $\alpha = 0.2$, and the transition temperature calculated with these parameters is $T_{c0} \sim 0.0255$, which is determined by the Ginzburg-Landau (GL) framework.

For the latter use, we define the normal-state Hamiltonian $H_N(\mathbf{k})$,

$$H_N(\mathbf{k}) = \begin{pmatrix} \xi(\mathbf{k}) - \mu_B H_z & \alpha(-\sin k_y - i \sin k_x) + i\mu_B H_y & t_{\perp} & 0 \\ \alpha(-\sin k_y + i \sin k_x) - i\mu_B H_y & \xi(\mathbf{k}) + \mu_B H_z & 0 & t_{\perp} \\ t_{\perp} & 0 & \xi(\mathbf{k}) - \mu_B H_z & \alpha(\sin k_y + i \sin k_x) + i\mu_B H_y \\ 0 & t_{\perp} & \alpha(\sin k_y - i \sin k_x) - i\mu_B H_y & \xi(\mathbf{k}) + \mu_B H_z \end{pmatrix}, \quad (8)$$

where $H_x = 0$ is abbreviated. For the centrosymmetric bilayers, we analyze the model introduced above. Furthermore, we will consider the effects of potential gradient which breaks global inversion symmetry. In the presence of the potential gradient v , the potential Hamil-

tonian H_v is added to $H_N(\mathbf{k})$ with

$$H_v = \begin{pmatrix} v & 0 & 0 & 0 \\ 0 & v & 0 & 0 \\ 0 & 0 & -v & 0 \\ 0 & 0 & 0 & -v \end{pmatrix}. \quad (9)$$

B. Ginzburg-Landau free energy

We calculate the GL free energy with the Hamiltonian introduced in the previous section. By expanding the free energy in terms of the order parameter, we obtain

$$F = -\frac{1}{\beta} \ln \text{tr} e^{-\beta \hat{H}} \\ = F_0 + V (\Delta_1^* \ \Delta_2^*) \hat{\alpha}(\mathbf{q}) \begin{pmatrix} \Delta_1 \\ \Delta_2 \end{pmatrix} + \mathcal{O}(\Delta^4). \quad (10)$$

Here, $\beta = 1/k_B T$ is the inverse temperature, and \mathbf{q} corresponds to the Cooper-pair momentum as introduced in Eq. (7). The matrix $\hat{\alpha}(\mathbf{q})$ corresponds to the GL coefficients,

$$\hat{\alpha}_{nm}(\mathbf{k}, \mathbf{q}) = \begin{pmatrix} |\langle u_n(\mathbf{k}, \mathbf{q}) | \varphi_1 | u_m^*(-\mathbf{k}, \mathbf{q}) \rangle|^2 & \langle u_m^*(-\mathbf{k}, \mathbf{q}) | \varphi_1^\dagger | u_n(\mathbf{k}, \mathbf{q}) \rangle \langle u_n(\mathbf{k}, \mathbf{q}) | \varphi_2 | u_m^*(-\mathbf{k}, \mathbf{q}) \rangle \\ \langle u_m^*(-\mathbf{k}, \mathbf{q}) | \varphi_2^\dagger | u_n(\mathbf{k}, \mathbf{q}) \rangle \langle u_n(\mathbf{k}, \mathbf{q}) | \varphi_1 | u_m^*(-\mathbf{k}, \mathbf{q}) \rangle & |\langle u_n(\mathbf{k}, \mathbf{q}) | \varphi_2 | u_m^*(-\mathbf{k}, \mathbf{q}) \rangle|^2 \end{pmatrix}, \quad (13)$$

with the Fermi-Dirac function $f(\epsilon) = 1/(e^{\beta\epsilon} + 1)$, eigenvalues and eigenstates of $H_N(\mathbf{k}, \mathbf{q}) = H_N(\mathbf{k} + \mathbf{q}/2)$, $\epsilon_n(\mathbf{k}, \mathbf{q})$ and $|u_n(\mathbf{k}, \mathbf{q})\rangle$, and form factors φ_1 and φ_2 ,

$$\varphi_1 = \begin{pmatrix} \varphi & 0 \\ 0 & 0 \end{pmatrix}, \quad \varphi_2 = \begin{pmatrix} 0 & 0 \\ 0 & \varphi \end{pmatrix}, \quad (14)$$

where $\varphi = \begin{pmatrix} 0 & 1 \\ -1 & 0 \end{pmatrix}$ is the two-by-two matrix in the spin space [77].

The second-order transition line from the normal to the superconducting states can be determined by using $\hat{\alpha}(\mathbf{q})$. Let us write its eigenequation as

$$\hat{\alpha}(\mathbf{q}) |\mu(\mathbf{q})\rangle = \alpha_\mu(\mathbf{q}) |\mu(\mathbf{q})\rangle. \quad (15)$$

Then, the superconducting transition occurs when the smallest eigenvalue $\alpha_\mu(\mathbf{q})$ among various \mathbf{q} and μ vanishes as lowering the temperature. We note that $\hat{\alpha}(\mathbf{q})$ is calculated with the normal-state Hamiltonian given in the previous section, and therefore takes into account the microscopic information of the system beyond a phenomenology. The transition line obtained in this way coincides with that determined from the mean-field theory.

The eigenstates of $\hat{\alpha}(0)$ correspond to the BCS and the PDW states in the system with inversion symmetry, while are represented by their superposition in the absence of the inversion symmetry (i.e., in the presence of the potential gradient v). Here, the BCS and PDW states are expressed as

$$|\text{BCS}\rangle = \frac{1}{\sqrt{2}} \begin{pmatrix} 1 \\ 1 \end{pmatrix}, \quad (16)$$

$$|\text{PDW}\rangle = \frac{1}{\sqrt{2}} \begin{pmatrix} -1 \\ 1 \end{pmatrix}. \quad (17)$$

and its components are given by

$$\alpha_{ij}(\mathbf{q}) = \frac{1}{U} \delta_{ij} - \frac{1}{2L_x L_y} \sum_{\mathbf{k}} \sum_{n,m} F_{nm}(\mathbf{k}, \mathbf{q}) (\hat{\alpha}_{nm}(\mathbf{k}, \mathbf{q}))_{ij}, \quad (11)$$

where L_x and L_y are the system dimensions in the x and y directions, respectively, and $F_{nm}(\mathbf{k}, \mathbf{q})$ and $\hat{\alpha}_{nm}(\mathbf{k}, \mathbf{q})$ are written as

$$F_{nm}(\mathbf{k}, \mathbf{q}) = \frac{f(\epsilon_n(\mathbf{k}, \mathbf{q})) - f(-\epsilon_m(-\mathbf{k}, \mathbf{q}))}{\epsilon_n(\mathbf{k}, \mathbf{q}) + \epsilon_m(-\mathbf{k}, \mathbf{q})}, \quad (12)$$

Generally speaking, these two states are mixed with each other for a finite \mathbf{q} , but it can be shown that the eigenstates of $\hat{\alpha}(\mathbf{q})$ remain to be $|\text{BCS}\rangle$ and $|\text{PDW}\rangle$ for the system in the perpendicular magnetic field (see Appendix A).

C. Time-dependent Ginzburg-Landau equation

To calculate the linear and nonlinear paraconductivities, we use the general formulas derived from the phenomenological time-dependent Ginzburg-Landau (TDGL) equation in the momentum space [62, 72–74],

$$\Gamma_0 \frac{\partial \psi_{\mathbf{q}}(t)}{\partial t} = -\alpha_{\mathbf{q}}(t) \psi_{\mathbf{q}}(t) + \zeta_{\mathbf{q}}(t), \quad (18)$$

where Γ_0 introduces the lifetime of Cooper pairs and $\zeta_{\mathbf{q}}(t)$ is the white noise,

$$\langle \zeta_{\mathbf{q}}^*(t) \zeta_{\mathbf{q}'}(t') \rangle = \frac{2\Gamma_0}{\beta V} \delta(t - t') \delta_{\mathbf{q}, \mathbf{q}'}. \quad (19)$$

In this paper, we assume that Γ_0 is independent of the temperature and the magnetic field and set Γ_0 to be unity, which does not affect the qualitative results as seen later. We can obtain the paraconductivity by expanding the excess current contributed by Cooper pairs with respect to the electric field by using the solution of the TDGL equation,

$$j_i = \sigma_{1s}^{ij} E_j + \sigma_{2s}^{ijk} E_j E_k + \mathcal{O}(E^3). \quad (20)$$

Here, the electric field is taken into account by introducing the vector potential $\mathbf{A}(t) = -\mathbf{E}t$ by $\hat{\alpha}_{\mathbf{q}}(t) = \hat{\alpha}_{\mathbf{q}-2\mathbf{A}(t)}$. The general formulas of the linear and non-

linear paraconductivities are expressed as follows [74],

$$\sigma_{1s}^{ij} = \frac{\Gamma_0}{\beta V} \sum_{\mathbf{q}} \sum_{\mu\nu} \frac{\text{Re}[\langle \mu | j_i | \nu \rangle \langle \nu | j_j | \mu \rangle]}{\alpha_\mu \alpha_\nu (\alpha_\mu + \alpha_\nu)}, \quad (21)$$

$$\sigma_{2s}^{ijk} = \frac{2\Gamma_0^2}{\beta V} \sum_{\mathbf{q}} \sum_{\mu\nu\lambda} \frac{J_{\mu\nu\lambda}^{ijk} (\alpha_\mu + \alpha_\nu + 2\alpha_\lambda)}{\alpha_\lambda (\alpha_\mu + \alpha_\nu) (\alpha_\mu + \alpha_\lambda)^2 (\alpha_\nu + \alpha_\lambda)^2}, \quad (22)$$

with suppressing the argument \mathbf{q} of quantities. Here, $J_{\mu\nu\lambda}^{ijk} = \text{Re}[\langle \mu | j_i | \nu \rangle \langle \nu | j_j | \lambda \rangle \langle \lambda | j_k | \mu \rangle]$, $j_i(\mathbf{q}) = -\partial_{A_i} \hat{\alpha}(\mathbf{q})$ and $V = L_x L_y$. In actual calculations, the contribution from the momentum around \mathbf{q} which gives the minimum eigenvalue of $\hat{\alpha}(\mathbf{q})$ is dominant. For this reason, we introduce the cutoff q_c to the momentum integral rather than to evaluate the contribution of every \mathbf{q} in the whole Brillouin zone. We numerically evaluate j_i by

$$-\partial_{A_i} \hat{\alpha}_{\mathbf{q}} = 2\partial_{q_i} \hat{\alpha}_{\mathbf{q}} = \frac{\hat{\alpha}_{\mathbf{q}+dq_i\hat{x}_i} - \hat{\alpha}_{\mathbf{q}-dq_i\hat{x}_i}}{dq_i} + \mathcal{O}(dq_i^2), \quad (23)$$

where $dq_i = 0.001$.

III. LINEAR PARACONDUCTIVITY IN THE PERPENDICULAR MAGNETIC FIELD

In this section, we investigate the superconducting phase diagram and linear paraconductivity in the perpendicular magnetic field. The system has the inversion symmetry

$$\mathcal{I} \hat{H}_N(\mathbf{k}, \mathbf{q}) \mathcal{I}^{-1} = \hat{H}_N(-\mathbf{k}, -\mathbf{q}), \quad (24)$$

with inversion operator $\mathcal{I} = \sigma_x \otimes \sigma_0$, when the potential gradient v is absent. The system also has a fourfold rotation symmetry, and thus we can write the linear paraconductivity as $\sigma_{1s}^{ij} = \delta_{ij} \sigma_{1s}$. In the following, we first consider the inversion symmetric system with $v = 0$ and subsequently consider the case with $v \neq 0$.

A. The system with inversion symmetry

We first consider the system with inversion symmetry $v = 0$. We calculate the superconducting transition line with the GL coefficient $\hat{\alpha}(\mathbf{q})$ and the first-order transition line by evaluating the mean-field free energy. In addition, we calculate the linear paraconductivity along the transition line between the normal and the superconducting states. Figure 1 shows the superconducting phase diagram and linear paraconductivity in this model. As shown in Figs. 1(a) and 1(b), wherein the different magnitudes of Rashba spin-orbit coupling α are adopted, the BCS state, whose order parameter is of the form $(\Delta_1, \Delta_2) = (+\Delta, +\Delta)$, is stable in the low magnetic field. On the other hand, the PDW state with

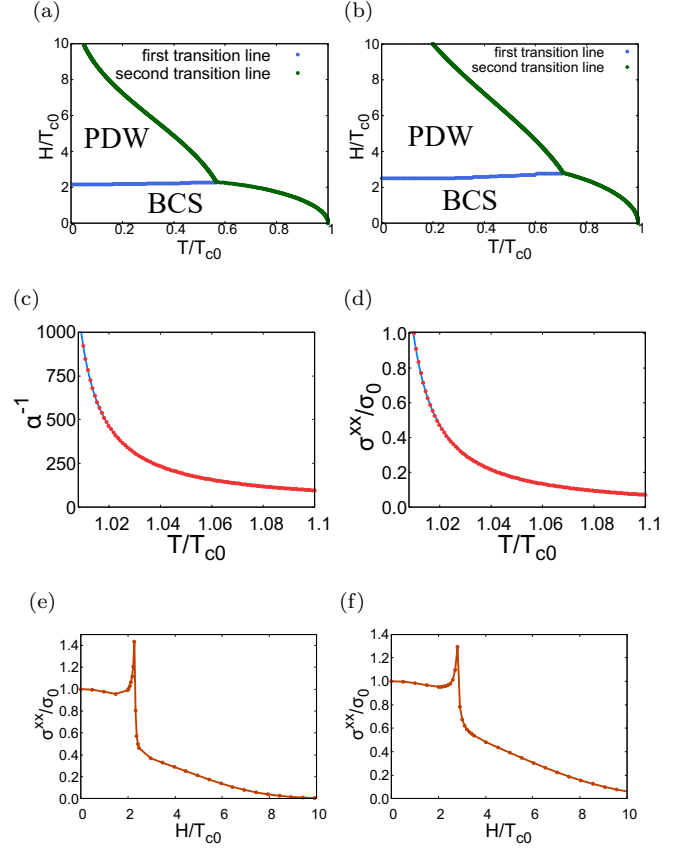


FIG. 1. (a-b,e-f) Phase diagram and linear paraconductivity of the system with inversion symmetry. (a) and (e) is the case of $\alpha = 0.2$ and (b) and (f) is the case of $\alpha = 0.3$. (c-d) Results of fitting for $\alpha_{\text{BCS}}^{-1}(0)$ and σ_{1s} with Eqs. (26) and (27). Fitting parameters are $(a_1, b_1) \sim (9.173, 4.543)$ and $(a_2, b_2) \sim (0.010, -0.035)$. We can see that α^{-1} and σ_{1s} are almost proportional to $(T - T_c(H))^{-1}$ near the transition temperature.

$(\Delta_1, \Delta_2) = (+\Delta, -\Delta)$ is stable in the high magnetic field. These results reproduce the known phase diagrams of the bilayer superconductor [64].

We calculate the linear paraconductivity along the transition line highlighted with green in Figs. 1(a) and 1(b). For each value of the magnetic field H , we adopt the temperature T ,

$$T - T_c(H) = \frac{T_c(0)}{100}, \quad (25)$$

which is slightly above the mean-field transition temperature. We use Eq. (25) for calculations of the linear and nonlinear paraconductivity in this paper unless otherwise specified. To check the validity of our calculations, we show the temperature dependence of $\alpha_{\text{BCS}}(0)^{-1}$ and σ_{1s} in Figs. 1(c) and 1(d), respectively. The results indicate that α_μ and σ_{1s} in the cases of $\alpha = 0.2$ and 0.3 with $\mu_B H = 0$ are well fitted by $\alpha_{\text{BCS}}(0)^{-1} \sim (T - T_c(H))^{-1}$, as they should be in two-dimensional su-

perconductors [69]. In this fitting, we assume,

$$\alpha_{\text{BCS}}^{-1}(0) = \frac{a_1}{(T - T_c(H))/T_{c0}} + b_1, \quad (26)$$

$$\frac{\sigma_{1s}}{\sigma_0} = \frac{a_2}{(T - T_c(H))/T_{c0}} + b_2, \quad (27)$$

with fitting parameters $(a_1, b_1), (a_2, b_2)$.

We see that the linear paraconductivity shows a peak near the BCS-PDW transition point in both cases of $\alpha = 0.2$ and $\alpha = 0.3$ in Figs. 1(e) and 1(f). These peaks stem from the degeneracy of the superconducting states at the BCS-PDW transition point. We can consider this in such a way that we can separate the paraconductivity to contributions of the BCS fluctuation and the PDW fluctuation as

$$\sigma_{1s} = \sigma_{\text{BCS}} + \sigma_{\text{PDW}} + \sigma_{\text{BCS-PDW}}. \quad (28)$$

Here, σ_{BCS} (σ_{PDW}) refers to the contribution with $\mu = \nu = \text{BCS}$ (PDW) in Eq. (21), while $\sigma_{\text{BCS-PDW}}$ represents the contribution with $\mu \neq \nu$ and vanishes in the perpendicular magnetic field as shown in Appendix A. To separately consider the BCS and PDW contributions, we show their putative transition lines and their contributions to the linear paraconductivity in Fig. 2. Here, the putative transition lines are determined by $\alpha_{\text{BCS}}(T, H) = 0$ for Figs. 2(a) and 2(e), and $\alpha_{\text{PDW}}(T, H) = 0$ for Figs. 2(c) and 2(g). As is clear from Figs. 2(b), 2(d), 2(f) and 2(h), both the BCS and PDW contributions take sizable values so that the linear paraconductivity is enhanced around the BCS-PDW transition point. Thus, the enhanced fluctuation due to the degeneracy of the BCS and PDW states is one of the main reasons for the peaked linear paraconductivity.

Figure 2(b) shows that the BCS contribution in the case of $\alpha = 0.2$ by itself has a peak at the BCS-PDW transition point. This provides another contribution to the peak structure of σ_{1s} in Fig. 1(e). The peak of σ_{BCS} stems from the Pauli paramagnetic depairing effect, which can be understood as follows. We show in Fig. 2(a) the putative critical magnetic field of the BCS state $H = H_{\text{BCS}}(T)$, which is defined by $\alpha_{\text{BCS}}(T, H_{\text{BCS}}(T)) = 0$. We also define the corresponding transition temperature by $\alpha_{\text{BCS}}(T_{\text{BCS}}(H), H) = 0$. The $H_{\text{BCS}}(T)$ line has a maximum, and we denote this point in the phase diagram by (T^*, H^*) . When we consider the region near (T^*, H^*) , α_{BCS} up to $\mathcal{O}(T - T_{\text{BCS}}(H))$,

$$\alpha_{\text{BCS}}(T, H) \simeq \left. \frac{\partial \alpha_{\text{BCS}}}{\partial T} \right|_{T_{\text{BCS}}(H), H} (T - T_{\text{BCS}}(H)), \quad (29)$$

is approximately proportional to $(H^* - H)$. This is because the coefficient satisfies

$$\frac{\partial \alpha_{\text{BCS}}}{\partial T} = - \frac{dH_{\text{BCS}}}{dT} \frac{\partial \alpha_{\text{BCS}}}{\partial H}, \quad (30)$$

on the transition line and thus vanishes at (T^*, H^*) , leading to the $H - H^*$ dependence when seen as a function

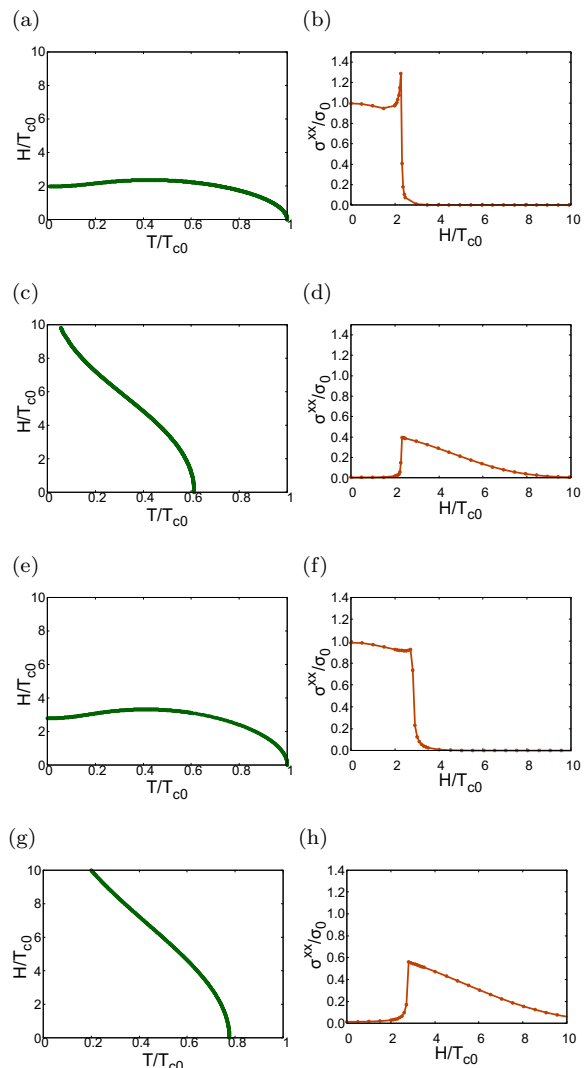


FIG. 2. Putative transition lines of the BCS and PDW states and the linear paraconductivity contributed from the BCS and PDW fluctuations. (a-d) The results for $\alpha = 0.2$ while (e-h) for $\alpha = 0.3$. (a) and (e) show the line $\alpha_{\text{BCS}} = 0$, and (b) and (f) show the BCS contribution to the linear paraconductivity, σ_{BCS} . (c) and (g) show the line $\alpha_{\text{PDW}} = 0$, and (d) and (h) are the PDW contribution to the linear paraconductivity, σ_{PDW} .

of the magnetic field H . This is confirmed by fitting the numerical results of α_{BCS}^{-1} with the functional form $\frac{a_3}{(H^* - H)/T_{c0}} + b_3$ and the fitting parameters a_3 and b_3 , as shown in Fig. 3(a). Thus, $\alpha_{\text{BCS}}(T, H)$ is small near (T^*, H^*) and naturally enhances the linear paraconductivity, giving rise to the peak structure. The maximum H^* of the putative BCS critical magnetic field is typically obtained in the phase diagram of the FFLO superconductivity [78]. The decreasing tendency of $\partial \alpha_{\text{BCS}} / \partial T \propto dH_{\text{BCS}} / dT$ along the transition line is considered to be a general feature of superconductors suffering the Pauli paramagnetic depairing effect, which are characterized

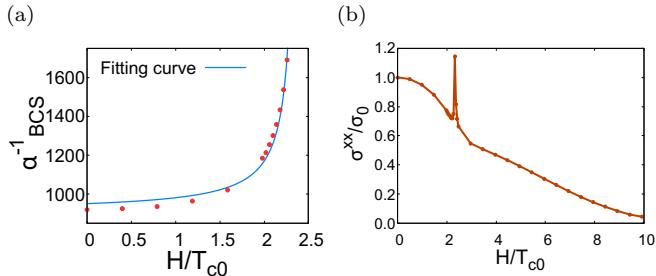


FIG. 3. (a) Fitting of the magnetic field dependence of α_{BCS}^{-1} . Fitting parameters are $(a_3, b_3) \sim (99.9, 909.8)$. (b) Linear paraconductivity calculated with $\Gamma_0 = \tau_0 N_0$ and $T - T_c(H) = T_c(H)/100$.

by the expression $H_{\text{BCS}}(T) \sim \sqrt{T_{\text{BCS}}(0) - T}$ for $T \sim T_{\text{BCS}}(0)$. Thus, the Pauli paramagnetic depairing effect is identified as the origin of the peaked σ_{BCS} , which is an origin of the peak in the paraconductivity.

Note that the contribution from the BCS state rapidly disappears after the BCS-PDW transition, because the actual transition temperature $T_c(H)$ goes away from the putative BCS transition temperature $T_{\text{BCS}}(H)$. In contrast to the case of $\alpha = 0.2$, the BCS-PDW transition point on the green line in Fig. 1(b) for $\alpha = 0.3$ is farther from (T^*, H^*) , so that the Pauli paramagnetic depairing effect is less significant in Fig. 2(f).

In contrast to the BCS contribution, the PDW contribution is least affected by the Pauli paramagnetic depairing effect. Consistent with this fact, we can see in Figs. 2(c), 2(d), 2(g), and 2(h) that its critical magnetic field does not have an extremum, and thus there is no sharp peak in σ_{PDW} like that in Fig. 2(b) [Figs. 2(d) and 2(h)]. Physically, this is attributed to the robustness of the PDW state against the Pauli depairing effect [64, 79], as is also manifest from its transition line extending in the high-magnetic field region compared with that of the BCS state.

Similarly to the BCS contribution, the PDW contribution is tiny in the low-magnetic field since $T_{\text{PDW}}(H)$, which is defined by $\alpha_{\text{PDW}}(T_{\text{PDW}}(H), H) = 0$ and shown in Figs. 2(c) and 2(g), is away from the true transition line $T_c(H)$ in Figs. 1(a) and 1(b). When the magnetic field is larger than the BCS-PDW transition point, on the other hand, there appears a sizable PDW contribution. According to Figs. 2(d) and 2(h), the PDW contribution decays slowly as increasing the magnetic field. This can be understood as follows. When we write $\alpha_{\text{PDW}}(\mathbf{q}) = N_{\text{PDW}}(\epsilon + \xi_{\text{PDW}}^2 q^2) + O(q^4)$, the linear paraconductivity in the high magnetic field can be written as $\sigma_{1s} \simeq \sigma_{\text{PDW}} \simeq \frac{\Gamma_0 T}{2\pi\epsilon N_{\text{PDW}}}$ [69, 74]. It turns out that T/N_{PDW} decreases as increasing H (data not shown), due to the decreasing $T_c(H)$. Note also that the reduced temperature $\epsilon = (T - T_c(H))/T_c(H)$ increases since $T - T_c(H)$ is fixed to $T_c(0)/100$. Thus, these two factors are responsible for the decreasing σ_{1s} in the high

magnetic field.

So far, we have discussed the linear paraconductivity by adopting the phenomenological relaxation parameter $\Gamma_0 = 1$. Another possible choice would be $\Gamma_0 = N_0 \tau_0$, where $\tau_0 = \pi/8T$ is the GL relaxation time [69] and it would be feasible to choose N_0 as $\partial_\epsilon \alpha_\mu(\mathbf{q})$ for the dominant superconducting state. We show in Fig. 3(b) the linear paraconductivity by assuming $\Gamma_0 = N_0 \tau_0$. The results follow the formula $\sigma_{1s} \simeq 1/16\epsilon$ [69] except near the BCS-PDW transition points. We can see that the qualitative results remain unchanged, accompanying the peak structure of σ_{1s} coming from the degenerate superconducting states.¹ We adopt $\Gamma_0 = 1$ in the rest of the paper.

The results obtained in this section suggest that we can experimentally detect the BCS-PDW phase transition by observing the enhancement of the linear paraconductivity. This would generally work as strong evidence for the degeneracy of the two different superconducting states not limited to the BCS and PDW states.

B. The system without inversion symmetry

Next, we discuss the system without inversion symmetry, which is broken by the application of the potential gradient v . We focus on how the behavior of the paraconductivity changes while changing the magnitude of v . To see this, we adopt two strengths of the potential gradient, $v = 0.01$ and $v = 0.05$. Considering that the transition temperature in the absence of both v and H is $T_{c0} \sim 0.0255$, these two cases correspond to weakly and strongly noncentrosymmetric superconductivity, respectively. The following discussion proceeds with $\alpha = 0.2$.

In the beginning, we calculate the superconducting transition line and show the results in Figs. 4(a) and 4(b). Due to the application of the potential gradient and the broken inversion symmetry, the first-order phase transition between the BCS and PDW states changes to the BCS-PDW crossover. This can be verified by writing the eigenstates as

$$|\alpha\rangle = \gamma |\text{BCS}\rangle + \delta |\text{PDW}\rangle, \quad (31)$$

and looking at the squared values of its coefficients. We can see the crossover in Figs. 4(c) and 4(d), where we find that the onset of the crossover regime in Fig. 4(d) is shifted to the higher magnetic field than Fig. 4(c) by increasing the potential gradient. By comparing the cases of $v = 0.01$ and $v = 0.05$, we can see that in the former case the kink point of $T_c(H)$ remains near the BCS-PDW

¹ Strictly speaking, the peak in σ_{1s} from the Pauli depairing effect would tend to cancel out with the contribution from N_0 . The other properties seem to be unaffected by the choice of Γ_0 . Note also that N_0 of the present choice is discontinuous at the BCS-PDW transition.

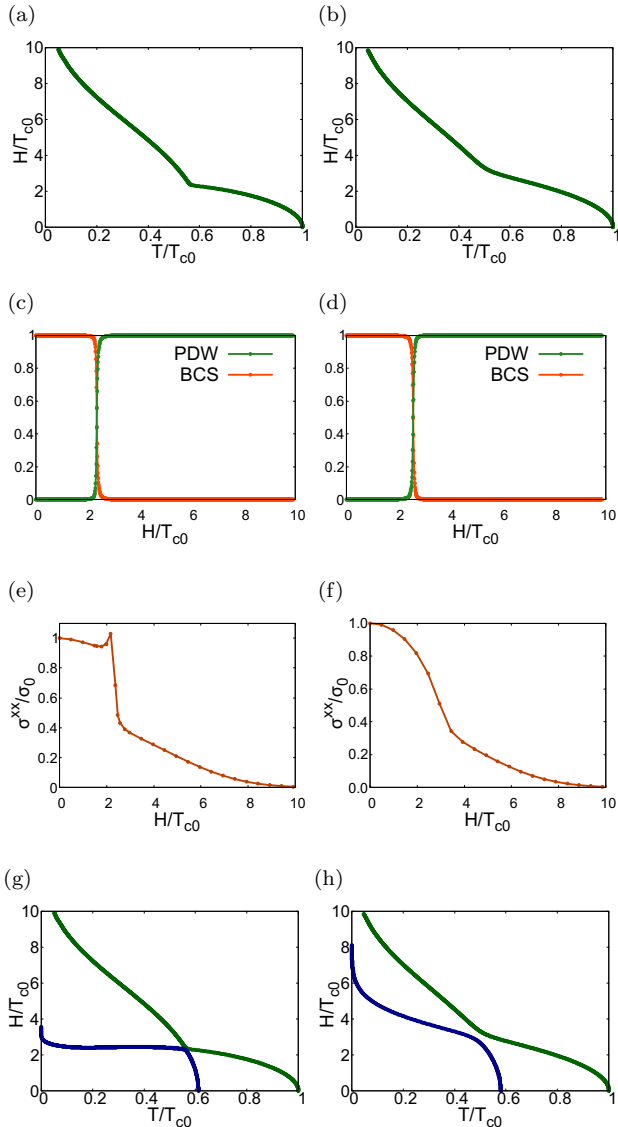


FIG. 4. (a-b) Superconducting transition line in the case of (a) $v = 0.01$ and (b) $v = 0.05$. (c-d) H -dependence of the BCS and PDW components of the order parameter. In both figures of (c) $v = 0.01$ and (d) $v = 0.05$, the BCS-PDW crossover occurs at $H/T_{c0} \sim 2$. (e-f) Linear paraconductivity for (e) $v = 0.01$ and (f) $v = 0.05$. (g-h) The putative transition lines defined by $\alpha_\mu = 0.0$. (g) $v = 0.01$ and (h) $v = 0.05$.

crossover area while in the latter case the kink changes to a smooth upturn. The difference between the two cases is attributed to the extent to which the degeneracy of the BCS and PDW states is lifted.

We show the linear paraconductivity of the system with the potential gradient in Figs. 4(e) and 4(f). It is shown that the linear paraconductivity has a peak accompanied by the BCS-PDW crossover for $v = 0.01$. Thus, the linear paraconductivity of the weakly noncentrosymmetric system resembles that of the centrosymmetric system, as expected. On the other hand, the

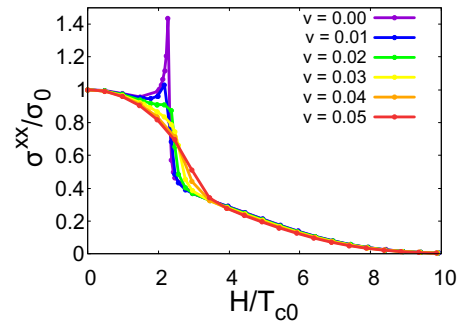


FIG. 5. Linear paraconductivity for various values of the potential gradient. It can be seen that the peaks are gradually suppressed.

peak of the paraconductivity disappears in the strongly noncentrosymmetric system $v = 0.05$. This seems to be correlated with the smoother transition line observed in Fig. 4(h) compared with that in Fig. 4(g). We show in Figs. 4(g) and 4(h) by green and blue lines the zero contour lines of the two eigenvalues of the GL coefficient $\hat{\alpha}$. The mixing of the BCS and PDW states, or in other words the avoided crossing of the two putative transition lines, clearly explains the presence and the absence of the approximate kink structure in the weak and strong potential gradients, respectively. The lifted degeneracy naturally suppresses the fluctuation in the sub-leading superconducting channel, resulting in the absence of the peak in linear conductivity in the strong potential gradient.

Lastly, we discuss the potential gradient dependence of the linear paraconductivity as shown in Fig. 5. We can see that the peak height is monotonically decreasing with increasing the strength of the potential gradient. The peak vanishes near

$$v \sim T_{c0}. \quad (32)$$

The linear paraconductivity in the high magnetic field is almost unaffected by the potential gradient, owing to the dominance of the PDW state. Experimental observation of the peaked conductivity and its decaying tendency under the application of the potential gradient will strongly support the superconducting multiphase.

IV. LINEAR AND NONLINEAR PARACONDUCTIVITY IN THE IN-PLANE MAGNETIC FIELD

In this section, we study the linear and nonlinear paraconductivity of the system in the in-plane magnetic field with and without the potential gradient.

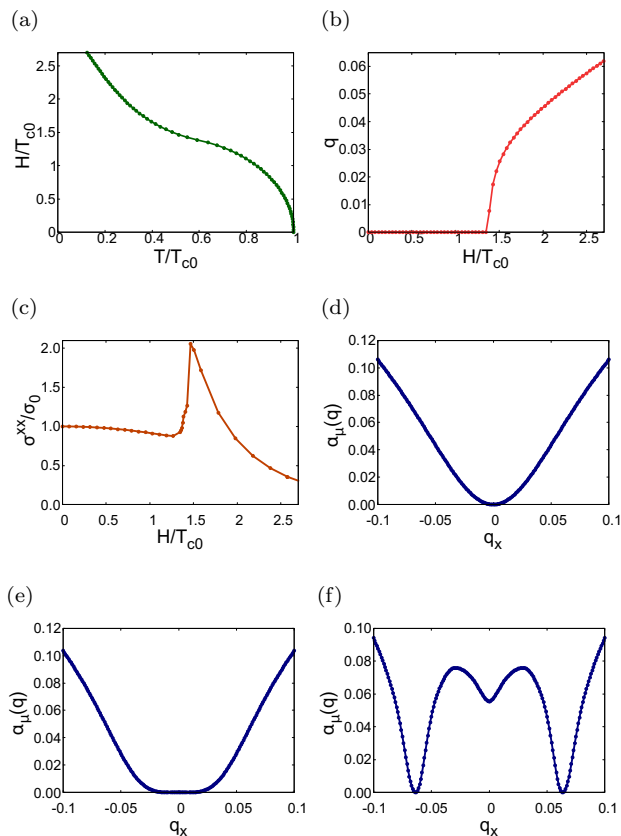


FIG. 6. (a) The superconducting transition line of the system in the in-plane magnetic field. (b) The magnetic field dependence of Cooper pair's momentum along the transition line. Superconducting state changes from the BCS state to the FFLO state near $H/T_{c0} \sim 1.4$. (c) The linear paraconductivity. (d-f) Momentum dependence of α_μ for $q_y = 0$. (d), (e), and (f) correspond to $H = 0.00$, 0.35 , and 0.70 , respectively.

A. The system with inversion symmetry

In the beginning, we consider the system without the potential gradient. In this case, the system has inversion symmetry, and therefore the nonlinear paraconductivity vanishes. We calculate the superconducting transition line and the linear paraconductivity in the same way as Sec. III.

As understood from Figs. 6(a) and 6(b), the superconducting phase diagram has the BCS phase in the low magnetic field and the FFLO phase in the high magnetic field [76]: The Cooper-pair momentum becomes finite for the magnetic field $H \gtrsim 1.4T_{c0}$. Furthermore, the linear paraconductivity σ_{1s}^{xx} has a peak near the tricritical point as shown in Fig. 6(c). The origin of this peak is attributed to the shape of $\alpha_\mu(\mathbf{q})$. We show the momentum dependence of $\alpha_\mu(\mathbf{q})$ for the system in the BCS phase ($H = 0.00$) and FFLO phase ($H = 0.70$) and near the tricritical point ($H = 0.35$), in Figs. 6(d), 6(f) and 6(e), respectively. It should be noted that the contribution

to the paraconductivity formula Eq. (21) mainly comes from the region where $\alpha_\mu(\mathbf{q})$ is vanishingly small. Near the tricritical point, we can see from Fig. 6(e) that the area of small $\alpha_\mu(\mathbf{q})$ is much larger than that in Figs. 6(d) and 6(f). This naturally leads to the peak of paraconductivity. In other words, the peaked paraconductivity near the tricritical point may be interpreted as coming from the degeneracy of the BCS and FFLO states, in analogy with the case in the perpendicular magnetic field. The result obtained here is consistent with the previous study which pointed out the enhanced linear paraconductivity with the anomalous temperature scaling near the tricritical point [70, 71]. This result implies that the observation of the linear paraconductivity can be used as a probe of FFLO superconductors.

B. The system without inversion symmetry

In this section, we apply the potential gradients $v = 0.01$ and $v = 0.10$, which are smaller and larger than the transition temperature $T_{c0} \sim 0.0255$, and correspond to weakly and strongly noncentrosymmetric superconductors, respectively. We consider not only the linear paraconductivity but also the nonlinear paraconductivity, which is allowed due to the broken inversion symmetry and C_{2z} rotation symmetry. As an indicator of the nonreciprocity, in addition to σ_{2s}^{xxx} , we focus on the quantity

$$\eta^{xxx} = \frac{\sigma_{2s}^{xxx}}{(\sigma_{1s}^{xx})^2}, \quad (33)$$

to study the nonreciprocal charge transport. This quantity is convergent as approaching the transition temperature, in contrast to σ_{1s} and σ_{2s} . It has the dimension of the inverse of the current density and, therefore, represents the typical value of the current density where nonreciprocity becomes visible [74].

We show the calculation results in Fig. 7. First, we discuss the difference of the superconducting phase diagrams in the presence and absence of the inversion symmetry, by comparing Figs. 6 and 7. By switching on the potential gradient v , due to the inversion symmetry breaking, the BCS-FFLO transition in Fig. 6 begins to change to the crossover of the so-called helical superconductivity [74, 80–90]. Indeed, the Cooper-pair momentum takes finite values in the low-field regime before it takes large values in the high magnetic field, as shown in Figs. 7(b) and 7(g). For clarity, we call the crossover in weakly and strongly noncentrosymmetric cases as BCS-FFLO-like crossover and helical crossover, respectively.

When the inversion symmetry breaking is weak ($v = 0.01$), the behavior of the linear paraconductivity in the moderate magnetic field is similar to that near the BCS-PDW transition. Indeed, we can see that the linear paraconductivity has a peak in the BCS-FFLO-like crossover region [Fig. 7(c)] as well as near the BCS-FFLO transition point [Fig. 6(c)]. By contrast, Fig. 7(h) shows that

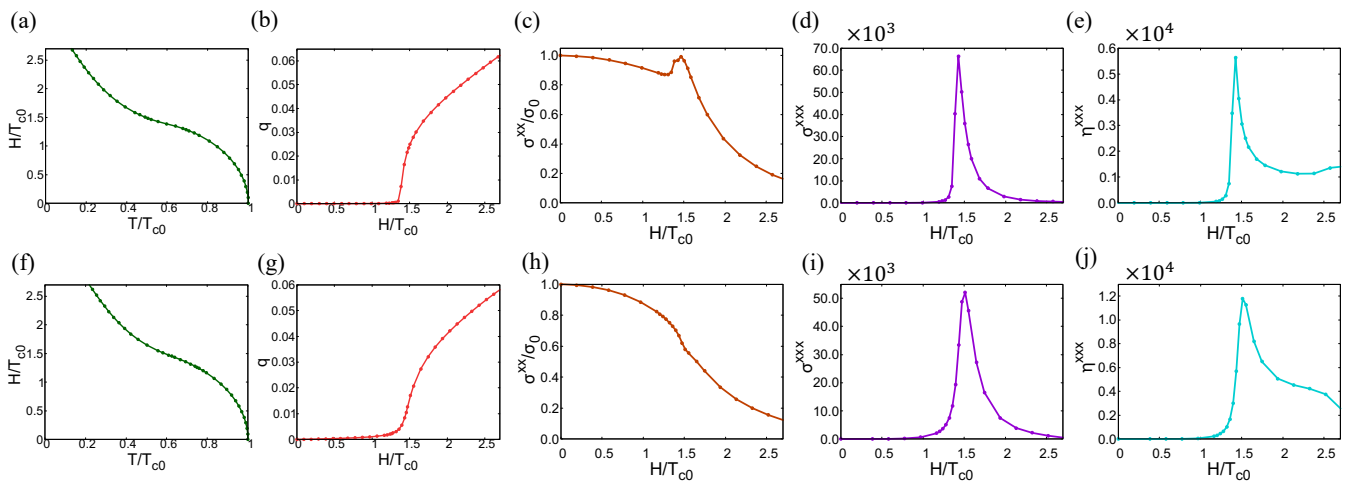


FIG. 7. The superconducting transition line [(a),(f)], Cooper-pair momentum [(b),(g)], linear [(c),(h)] and nonlinear [(d),(i)] paraconductivities, and nonreciprocity [(e),(j)] of the system in the in-plane magnetic field and potential gradient. (a-e) show the results of $v = 0.01$ and (f-j) are the results of $v = 0.10$.

the peak vanishes in the strongly noncentrosymmetric system, i.e., in the helical crossover regime. These are natural results because the peaked linear paraconductivity signals the degenerate superconducting states and the degeneracy is sufficiently lifted in the strongly noncentrosymmetric case in Fig. 7(h).

Interestingly, the behavior of the nonlinear paraconductivity is significantly different from the linear paraconductivity. We can see in Figs. 7(d) and 7(i) that there is a peak in the nonlinear paraconductivity in both weakly and strongly noncentrosymmetric systems with comparable strengths of σ_{2s}^{xxx} and η^{xxx} . The obtained peak in strongly noncentrosymmetric superconductors is consistent with the results of Ref. [74], which studies the enhancement of nonlinear paraconductivity associated with the helical crossover in a strongly noncentrosymmetric mono-layer Rashba model. Our results indicate that the enhanced nonlinear paraconductivity associated with the evolution of finite-momentum superconductivity also exists in the weakly noncentrosymmetric regime.

To understand the behavior of the nonlinear paraconductivity, we show in Figs. 8 and 9 the momentum dependence of $\alpha_\mu(\mathbf{q})$ with $\mathbf{q} = (q_x, 0)$ in the moderate and strong magnetic fields. Here, μ specifies the minimum eigenvalue of $\hat{a}(\mathbf{q})$. These figures clearly show the realization of finite-momentum superconductivity in the in-plane magnetic field. The results of $\alpha_\mu(\mathbf{q})$ for $v = 0.01$ is similar to those of the FFLO state shown in Figs. 6(e) and 6(f), reflecting the weak inversion breaking ($v \ll T_{c0}$), while the strongly noncentrosymmetric case ($v \gg T_{c0}$) in Figs. 8(c) and 8(d) shows a large deviation. We also show in Figs. 9(a) and 9(b) the enlarged figures of Figs. 8(a) and 8(c), respectively, to consider the main contribution to the paraconductivity coming from the region $\alpha_\mu(\mathbf{q}) \sim 0$. When seen in this energy scale,

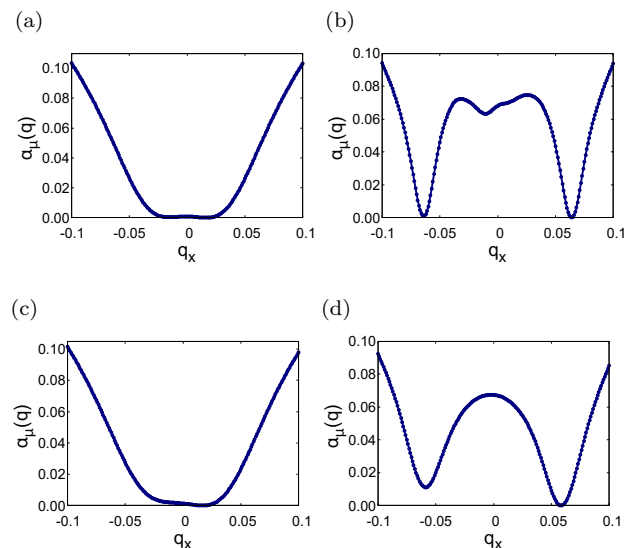


FIG. 8. The momentum dependence of $\alpha_\mu(\mathbf{q})$. (a) and (b) are the case of $v = 0.01$, while (c) and (d) are the case of $v = 0.10$. (a) and (c) are for the moderate magnetic field $H = 0.036$ and $H = 0.039$, respectively, where the nonlinear paraconductivity shows the peak. (b) and (d) are obtained in the high magnetic field, $H = 0.070$.

the structure of $\alpha_\mu(\mathbf{q})$ for $v = 0.01$ is essentially the same as that for $v = 0.1$. Actually, the values of $\alpha_\mu(\mathbf{q})$ at the local minima $q \sim \pm 0.02$, dubbed α_\pm , are not degenerate due to the inversion symmetry breaking $v = 0.01 \neq 0$, and satisfy $\alpha_- - \alpha_+ \gg \alpha_+ \gtrsim 0$. This means that the α_+ valley mainly contributes to the nonlinear paraconductivity in the same way as the strongly noncentrosymmetric case. Thus, at the temperatures considered here, the sys-

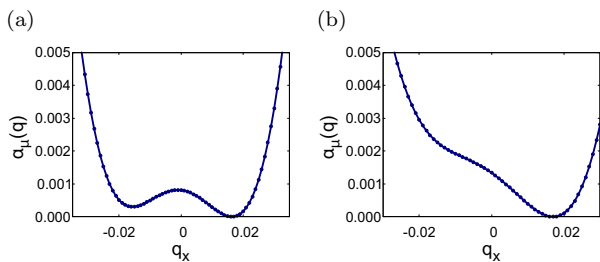


FIG. 9. Enlarged figures of Figs. 8(a) and 8(c) for small $\alpha_\mu(\mathbf{q})$. The panels (a) and (b) correspond to Figs. 8(a) and 8(c), respectively.

tem is sufficiently noncentrosymmetric for the nonlinear paraconductivity even though $v \ll T_{c0}$. This explains the appearance of the peaked nonlinear paraconductivity in Fig. 7(d). We expect that the peak width will decrease when v is decreased from $v = 0.01$ with fixing the reduced temperature, and eventually will vanish when $\alpha_- - \alpha_+ \sim \alpha_+$ is always satisfied along the transition line. This is consistent with $\sigma_{2s}^{xxx} = 0$ at $v = 0$ as enforced by the inversion symmetry.

The important point is that a small potential gradient $v \ll T_{c0}$ is sufficient to obtain the sizable nonlinear paraconductivity. Such a small v does not usually modify superconducting properties. In this case, on the other hand, each valley of the FFLO state shown e.g., in Fig. 6(f), has the intrinsic nonreciprocity even without v : The $\alpha_\mu(\mathbf{q})$ dispersion has a (cubic) asymmetry with respect to each local minimum, which has been identified as the origin of the nonreciprocal charge transport in noncentrosymmetric superconductors [62, 72–74]. The application of the potential gradient lifts the degeneracy of the two valleys, and one of the valleys selectively contributes to the nonlinear paraconductivity, picking up the intrinsic nonreciprocity of finite-momentum Cooper pairs. A small potential gradient inevitably exists in most thin film superconductors owing to substrate effects. Since the other contributions to the nonlinear paraconductivity unrelated to the FFLO state, if any, would be small when $v \ll T_{c0}$, the observation of the peaked nonlinear paraconductivity in intrinsically centrosymmetric superconductors under a small potential gradient serves as the strong evidence for the FFLO state.

V. SUMMARY AND CONCLUSION

In this study, we have investigated the linear and nonlinear paraconductivity in the bilayer system under the perpendicular and in-plane magnetic fields. We have revealed that the linear paraconductivity has a peak accompanied by the BCS-PDW transition in the system with a perpendicular magnetic field. The peak of linear paraconductivity tends to vanish by applying the potential gradient, signaling the lifted degeneracy of the BCS

and PDW states. Similar results of the linear paraconductivity are obtained for the in-plane magnetic field. In this case, the degeneracy of the BCS and FFLO states gives rise to the peak structure of the linear paraconductivity, which is also smeared out by applying the strong potential gradient. We have also studied the nonlinear paraconductivity of the system in the in-plane magnetic field. In contrast to the linear paraconductivity, a peak appears robustly in both the weakly and strongly noncentrosymmetric cases, i.e., both near the BCS-FFLO-like crossover and the helical crossover regions.

Since we neglected the orbital magnetic field in this paper, our results, particularly those in the perpendicular magnetic field, apply to the superconductors with large Maki parameters. Even when the orbital magnetic field can not be neglected, the qualitative results such as the peaked linear paraconductivity are expected to be unaffected. The peaked nonlinear paraconductivity in finite-momentum superconductors is also expected to survive to some extent in the orbital magnetic field [74], leaving a quantitative study as a future issue.

Based on the results obtained in this paper, we propose to use linear and nonlinear paraconductivity to probe multiphase and/or finite-momentum superconductors. In particular, this proposal is expected to be useful in thin film superconductors because the thermodynamic measurements are challenging there. The linear and nonlinear paraconductivity have different advantages and disadvantages. The linear paraconductivity can generally be used to probe degenerate superconducting states, through the detection of the peak structure, while it seems not sensitive to the detailed nature of the superconducting states. The nonlinear paraconductivity can only be used by breaking the inversion symmetry. However, once the symmetry allows a finite response, it can provide strong evidence for the finite-momentum superconductivity, including (nearly-)FFLO and helical superconducting states. A sizable response is obtained by lifting the degeneracy of the finite-momentum Cooper pairs. It is known that there are a variety of finite-momentum superconducting states such as the layer-decoupled state or the orbital FFLO state [59, 91–93], and pair-density-wave state in strongly correlated superconductors [94] (referring to a different state from the that studied in this paper, accompanying the in-plane modulation of the order parameter). It is an interesting future issue to quantitatively study the nonreciprocal charge transport of such finite momentum superconductors.

ACKNOWLEDGMENTS

T.M. thank fruitful discussion with Sho Ishikawa. This work was supported by JSPS KAKENHI No. JP21K13880, No. JP22H01181, No. JP22H04933, No. JP22H04476, No. JP23K17353, No. JP23K22452, No. JP24H00007, and No. JP24H01662.

- [1] M. Sigrist and K. Ueda, Phenomenological theory of unconventional superconductivity, *Rev. Mod. Phys.* **63**, 239 (1991).
- [2] X.-L. Qi and S.-C. Zhang, Topological insulators and superconductors, *Rev. Mod. Phys.* **83**, 1057 (2011).
- [3] Y. Tanaka, M. Sato, and N. Nagaosa, Symmetry and topology in superconductors –Odd-Frequency pairing and edge states–, *J. Phys. Soc. Jpn.* **81**, 011013 (2012).
- [4] M. Sato and S. Fujimoto, Majorana fermions and topology in superconductors, *J. Phys. Soc. Jpn.* **85**, 072001 (2016).
- [5] M. Sato and Y. Ando, Topological superconductors: a review, *Rep. Prog. Phys.* **80**, 076501 (2017).
- [6] S. Khim, J. F. Landaeta, J. Banda, N. Bannor, M. Brando, P. M. R. Brydon, D. Hafner, R. Kuchler, R. Cardoso-Gil, U. Stockert, A. P. Mackenzie, D. F. Agterberg, C. Geibel, and E. Hassinger, Field-induced transition within the superconducting state of CeRh_2As_2 , *Science* **373**, 1012 (2021).
- [7] S. Onishi, U. Stockert, S. Khim, J. Banda, M. Brando, and E. Hassinger, Low-Temperature thermal conductivity of the Two-Phase superconductor CeRh_2As_2 , *Frontiers in Electronic Materials* **2**, 10.3389/femat.2022.880579 (2022).
- [8] J. F. Landaeta, P. Khanenko, D. C. Cavanagh, C. Geibel, S. Khim, S. Mishra, I. Sheikin, P. M. R. Brydon, D. F. Agterberg, M. Brando, and E. Hassinger, Field-Angle dependence reveals Odd-Parity superconductivity in CeRh_2As_2 , *Phys. Rev. X* **12**, 031001 (2022).
- [9] S. Ogata, S. Kitagawa, K. Kinjo, K. Ishida, M. Brando, E. Hassinger, C. Geibel, and S. Khim, Parity transition of Spin-Singlet superconductivity using sublattice degrees of freedom, *Phys. Rev. Lett.* **130**, 166001 (2023).
- [10] H. Siddiquee, Z. Rehfuss, C. Broyles, and S. Ran, Pressure dependence of superconductivity in CeRh_2As_2 , *Phys. Rev. B Condens. Matter* **108**, L020504 (2023).
- [11] D. Möckli and A. Ramires, Two scenarios for superconductivity in CeRh_2As_2 , *Phys. Rev. Res.* **3**, 023204 (2021).
- [12] E. G. Schertenleib, M. H. Fischer, and M. Sigrist, Unusual - phase diagram of CeRh_2As_2 : The role of staggered noncentrosymmetry, *Phys. Rev. Res.* **3**, 023179 (2021).
- [13] A. Skuratovska, M. Sigrist, and M. H. Fischer, Spin response and topology of a staggered-rashba superconductor, *Phys. Rev. Res.* **3**, 033133 (2021).
- [14] T. Hazra and P. Coleman, Triplet pairing mechanisms from Hund’s-Kondo models: Applications to UTe_2 and CeRh_2As_2 , *Phys. Rev. Lett.* **130**, 136002 (2023).
- [15] S.-I. Kimura, J. Sichelschmidt, and S. Khim, Optical study of the electronic structure of locally noncentrosymmetric CeRh_2As_2 , *Phys. Rev. B Condens. Matter* **104**, 245116 (2021).
- [16] J. Ishizuka, K. Nogaki, M. Sigrist, and Y. Yanase, Correlation-induced fermi surface evolution and topological crystalline superconductivity in cerh_2as_2 , *arXiv:2312.07053 [cond-mat.supr-con]* (2023).
- [17] K. Nogaki, A. Daido, J. Ishizuka, and Y. Yanase, Topological crystalline superconductivity in locally noncentrosymmetric CeRh_2As_2 , *Phys. Rev. Res.* **3**, L032071 (2021).
- [18] K. Nogaki and Y. Yanase, Even-odd parity transition in strongly correlated locally noncentrosymmetric superconductors: Application to CeRh_2As_2 , *Phys. Rev. B Condens. Matter* **106**, L100504 (2022).
- [19] C. Lee and S. B. Chung, Linear optical response from the odd-parity Bardasis-Schrieffer mode in locally non-centrosymmetric superconductors, *Communications Physics* **6**, 1 (2023).
- [20] D. C. Cavanagh, T. Shishidou, M. Weinert, P. M. R. Brydon, and D. F. Agterberg, Nonsymmorphic symmetry and field-driven odd-parity pairing in CeRh_2As_2 , *Phys. Rev. B Condens. Matter* **105**, L020505 (2022).
- [21] K. Nogaki and Y. Yanase, Field-induced superconductivity mediated by odd-parity multipole fluctuation, *arXiv:2312.07053 [cond-mat.supr-con]* (2023).
- [22] S. Ran, C. Eckberg, Q.-P. Ding, Y. Furukawa, T. Metz, S. R. Saha, I.-L. Liu, M. Zic, H. Kim, J. Paglione, and N. P. Butch, Nearly ferromagnetic spin-triplet superconductivity, *Science* **365**, 684 (2019).
- [23] D. Aoki, J.-P. Brison, J. Flouquet, K. Ishida, G. Knebel, Y. Tokunaga, and Y. Yanase, Unconventional superconductivity in UTe_2 , *Journal of Physics: Condensed Matter* **34**, 243002 (2022).
- [24] S. Ran, I.-L. Liu, Y. S. Eo, D. J. Campbell, P. M. Neves, W. T. Fuhrman, S. R. Saha, C. Eckberg, H. Kim, D. Graf, F. Balakirev, J. Singleton, J. Paglione, and N. P. Butch, Extreme magnetic field-boosted superconductivity, *Nat. Phys.* **15**, 1250 (2019).
- [25] S. Ran, H. Kim, I.-L. Liu, S. R. Saha, I. Hayes, T. Metz, Y. S. Eo, J. Paglione, and N. P. Butch, Enhancement and reentrance of spin triplet superconductivity in ute_2 under pressure, *Phys. Rev. B* **101**, 140503 (2020).
- [26] L. Miao, S. Liu, Y. Xu, E. C. Kotta, C.-J. Kang, S. Ran, J. Paglione, G. Kotliar, N. P. Butch, J. D. Denlinger, and L. A. Wray, Low energy band structure and symmetries of UTe_2 from Angle-Resolved photoemission spectroscopy, *Phys. Rev. Lett.* **124**, 076401 (2020).
- [27] W.-C. Lin, D. J. Campbell, S. Ran, I.-L. Liu, H. Kim, A. H. Nevidomskyy, D. Graf, N. P. Butch, and J. Paglione, Tuning magnetic confinement of spin-triplet superconductivity, *npj Quantum Materials* **5**, 1 (2020).
- [28] D. Aoki, A. Nakamura, F. Honda, D. Li, Y. Homma, Y. Shimizu, Y. J. Sato, G. Knebel, J.-P. Brison, A. Pourret, D. Braithwaite, G. Lapertot, Q. Niu, M. Vališka, H. Harima, and J. Flouquet, Unconventional superconductivity in heavy fermion UTe_2 , *J. Phys. Soc. Jpn.* **88**, 043702 (2019).
- [29] D. Aoki, F. Honda, G. Knebel, D. Braithwaite, A. Nakamura, D. Li, Y. Homma, Y. Shimizu, Y. J. Sato, J.-P. Brison, and J. Flouquet, Multiple superconducting phases and unusual enhancement of the upper critical field in UTe_2 , *J. Phys. Soc. Jpn.* **89**, 053705 (2020).
- [30] D. Aoki, M. Kimata, Y. J. Sato, G. Knebel, F. Honda, A. Nakamura, D. Li, Y. Homma, Y. Shimizu, W. Knafo, D. Braithwaite, M. Vališka, A. Pourret, J.-P. Brison, and J. Flouquet, Field-Induced superconductivity near the superconducting critical pressure in UTe_2 , *J. Phys. Soc. Jpn.* **90**, 074705 (2021).
- [31] D. Aoki, H. Sakai, P. Opletal, Y. Tokiwa, J. Ishizuka, Y. Yanase, H. Harima, A. Nakamura, D. Li, Y. Homma, Y. Shimizu, G. Knebel, J. Flouquet, and Y. Haga, First observation of the de Haas-van alphen effect and fermi

- surfaces in the unconventional superconductor UTe_2 , *J. Phys. Soc. Jpn.* **91**, 083704 (2022).
- [32] G. Knebel, M. Kimata, M. Vališka, F. Honda, D. Li, D. Braithwaite, G. Lapertot, W. Knafo, A. Pourret, Y. J. Sato, Y. Shimizu, T. Kihara, J.-P. Brison, J. Flouquet, and D. Aoki, Anisotropy of the upper critical field in the Heavy-Fermion superconductor UTe_2 under pressure, *J. Phys. Soc. Jpn.* **89**, 053707 (2020).
- [33] H. Sakai, Y. Tokiwa, P. Opletal, M. Kimata, S. Awaji, T. Sasaki, D. Aoki, S. Kambe, Y. Tokunaga, and Y. Haga, Field induced multiple superconducting phases in UTe_2 along hard magnetic axis, *Phys. Rev. Lett.* **130**, 196002 (2023).
- [34] Y. Tokiwa, P. Opletal, H. Sakai, K. Kubo, E. Yamamoto, S. Kambe, M. Kimata, S. Awaji, T. Sasaki, D. Aoki, Y. Tokunaga, and Y. Haga, Stabilization of superconductivity by metamagnetism in an easy-axis magnetic field on ute_2 , [arXiv:2312.07053 \[cond-mat.supr-con\]](https://arxiv.org/abs/2312.07053) (2022).
- [35] H. Matsumura, H. Fujibayashi, K. Kinjo, S. Kitagawa, K. Ishida, Y. Tokunaga, H. Sakai, S. Kambe, A. Nakamura, Y. Shimizu, Y. Homma, D. Li, F. Honda, and D. Aoki, Large reduction in the a-axis knight shift on UTe_2 with $T_c = 2.1$ K, *J. Phys. Soc. Jpn.* **92**, 063701 (2023).
- [36] K. Kinjo, H. Fujibayashi, H. Matsumura, F. Hori, S. Kitagawa, K. Ishida, Y. Tokunaga, H. Sakai, S. Kambe, A. Nakamura, Y. Shimizu, Y. Homma, D. Li, F. Honda, and D. Aoki, Superconducting spin reorientation in spin-triplet multiple superconducting phases of UTe_2 , *Sci Adv* **9**, eadg2736 (2023).
- [37] S. Suetsugu, M. Shimomura, M. Kamimura, T. Asaba, H. Asaeda, Y. Kosuge, Y. Sekino, S. Ikemori, Y. Kasahara, Y. Kohsaka, M. Lee, Y. Yanase, H. Sakai, P. Opletal, Y. Tokiwa, Y. Haga, and Y. Matsuda, Fully gapped pairing state in spin-triplet superconductor UTe_2 , *Sci Adv* **10**, eadk3772 (2024).
- [38] D. Braithwaite, M. Vališka, G. Knebel, G. Lapertot, J.-P. Brison, A. Pourret, M. E. Zhitomirsky, J. Flouquet, F. Honda, and D. Aoki, Multiple superconducting phases in a nearly ferromagnetic system, *Communications Physics* **2**, 1 (2019).
- [39] A. Rosuel, C. Marcenat, G. Knebel, T. Klein, A. Pourret, N. Marquardt, Q. Niu, S. Rousseau, A. Demuer, G. Seyfarth, G. Lapertot, D. Aoki, D. Braithwaite, J. Flouquet, and J. P. Brison, Field-Induced tuning of the pairing state in a superconductor, *Phys. Rev. X* **13**, 011022 (2023).
- [40] S. M. Thomas, F. B. Santos, M. H. Christensen, T. Asaba, F. Ronning, J. D. Thompson, E. D. Bauer, R. M. Fernandes, G. Fabbris, and P. F. S. Rosa, Evidence for a pressure-induced antiferromagnetic quantum critical point in intermediate-valence UTe_2 , *Science Advances* **6**, eabc8709 (2020).
- [41] P. F. S. Rosa, A. Weiland, S. S. Fender, B. L. Scott, F. Ronning, J. D. Thompson, E. D. Bauer, and S. M. Thomas, Single thermodynamic transition at 2 K in superconducting UTe_2 single crystals, *Communications Materials* **3**, 1 (2022).
- [42] J. Ishizuka, S. Sumita, A. Daido, and Y. Yanase, Insulator-Metal transition and topological superconductivity in UTe_2 from a First-Principles calculation, *Phys. Rev. Lett.* **123**, 217001 (2019).
- [43] J. Tei, T. Mizushima, and S. Fujimoto, Possible realization of topological crystalline superconductivity with time-reversal symmetry in UTe_2 , *Phys. Rev. B Condens. Matter* **107**, 144517 (2023).
- [44] J. Tei, T. Mizushima, and S. Fujimoto, Pairing symmetries of multiple superconducting phases in UTe_2 : Competition between ferromagnetic and antiferromagnetic fluctuations, *Phys. Rev. B Condens. Matter* **109**, 064516 (2024).
- [45] R. Hakuno, K. Nogaki, and Y. Yanase, Magnetism and superconductivity in mixed-dimensional periodic anderson model for UTe_2 , *Phys. Rev. B Condens. Matter* **109**, 104509 (2024).
- [46] M. Naritsuka, T. Terashima, and Y. Matsuda, Controlling unconventional superconductivity in artificially engineered d-electron kondo superlattices, *J. Phys. Condens. Matter* **33**, 0 (2021).
- [47] J.-H. She and A. V. Balatsky, Berezinskii-Kosterlitz-Thouless transition to the superconducting state of heavy-fermion superlattices, *Phys. Rev. Lett.* **109**, 077002 (2012).
- [48] Y. Yanase, A. Daido, K. Takasan, and T. Yoshida, Topological d-wave superconductivity in two dimensions, *Physica E* **140**, 115143 (2022).
- [49] T. Asaba, M. Naritsuka, H. Asaeda, Y. Kosuge, S. Ikemori, S. Suetsugu, Y. Kasahara, Y. Kohsaka, T. Terashima, A. Daido, Y. Yanase, and Y. Matsuda, Evidence for a finite-momentum cooper pair in tricolor d-wave superconducting superlattices, *Nat. Commun.* **15**, 3861 (2024).
- [50] P. Fulde and R. A. Ferrell, Superconductivity in a strong spin-exchange field, *Phys. Rev.* **135**, A550 (1964).
- [51] A. I. Larkin and Y. N. Ovchinnikov, Nonuniform state of superconductors, *Zh. Eksp. Teor. Fiz.* **47**, 1136 (1964), [*Sov. Phys. JETP* **20**, 762 (1965)].
- [52] S. Nagata, T. Aochi, T. Abe, S. Ebisu, T. Hagino, Y. Seki, and K. Tsutsumi, Superconductivity in the layered compound 2H-TaS_2 , *J. Phys. Chem. Solids* **53**, 1259 (1992).
- [53] E. Navarro-Moratalla, J. O. Island, S. Mañas-Valero, E. Pinilla-Cienfuegos, A. Castellanos-Gomez, J. Qereda, G. Rubio-Bollinger, L. Chirolli, J. A. Silva-Guillén, N. Agraït, G. A. Steele, F. Guinea, H. S. J. van der Zant, and E. Coronado, Enhanced superconductivity in atomically thin TaS_2 , *Nat. Commun.* **7**, 11043 (2016).
- [54] Y. Yang, S. Fang, V. Fatemi, J. Ruhman, E. Navarro-Moratalla, K. Watanabe, T. Taniguchi, E. Kaxiras, and P. Jarillo-Herrero, Enhanced superconductivity upon weakening of charge density wave transport in $-\text{TaS}_2$ in the two-dimensional limit, *Phys. Rev. B Condens. Matter* **98**, 035203 (2018).
- [55] J. Bekaert, E. Khestanova, D. G. Hopkinson, J. Birkbeck, N. Clark, M. Zhu, D. A. Bandurin, R. Gorbachev, S. Fairclough, Y. Zou, M. Hamer, D. J. Terry, J. J. P. Peters, A. M. Sanchez, B. Partoens, S. J. Haigh, M. V. Milošević, and I. V. Grigorieva, Enhanced superconductivity in Few-Layer TaS_2 due to healing by oxygenation, *Nano Lett.* **20**, 3808 (2020).
- [56] A. Almoalem, I. Feldman, M. Shlafman, Y. E. Yaish, M. H. Fischer, M. Moshe, J. Ruhman, and A. Kanigel, Evidence of a two-component order parameter in $4\text{h}\text{-}\text{TaS}_2$ in the little-parks effect, [arXiv:2312.07053 \[cond-mat.supr-con\]](https://arxiv.org/abs/2312.07053) (2022).
- [57] Z. Wan, G. Qiu, H. Ren, Q. Qian, D. Xu, J. Zhou, J. Zhou, B. Zhou, L. Wang, Y. Huang, K. L. Wang, and X. Duan, Signatures of chiral superconductivity

- ity in chiral molecule intercalated tantalum disulfide, [arXiv:2312.07053 \[cond-mat.supr-con\]](https://arxiv.org/abs/2312.07053) (2023).
- [58] M. H. Fischer, P. A. Lee, and J. Ruhman, Mechanism for π phase shifts in Little-Parks experiments: Application to Hb-TaS₂ and to -TaS₂ intercalated with chiral molecules, *Phys. Rev. B Condens. Matter* **108**, L180505 (2023).
- [59] P. Wan, O. Zheliuk, N. F. Q. Yuan, X. Peng, L. Zhang, M. Liang, U. Zeitler, S. Wiedmann, N. E. Hussey, T. T. M. Palstra, and J. Ye, Orbital Fulde-Ferrell-Larkin-Ovchinnikov state in an ising superconductor, *Nature*, **1** (2023).
- [60] Y. Tokura and N. Nagaosa, Nonreciprocal responses from non-centrosymmetric quantum materials, *Nat. Commun.* **9**, 3740 (2018).
- [61] T. Ideue and Y. Iwasa, Symmetry breaking and nonlinear electric transport in van der waals nanostructures, *Annu. Rev. Condens. Matter Phys.* **12**, 201 (2021).
- [62] S. Hoshino, R. Wakatsuki, K. Hamamoto, and N. Nagaosa, Nonreciprocal charge transport in two-dimensional noncentrosymmetric superconductors, *Phys. Rev. B Condens. Matter* **98**, 054510 (2018).
- [63] N. Nagaosa and Y. Yanase, Nonreciprocal transport and optical phenomena in quantum materials, *Ann. Rev. Condens. Matter Phys.* **15**, 63 (2024).
- [64] T. Yoshida, M. Sigrist, and Y. Yanase, Pair-density wave states through spin-orbit coupling in multilayer superconductors, *Phys. Rev. B Condens. Matter* **86**, 134514 (2012).
- [65] D. Maruyama, M. Sigrist, and Y. Yanase, Locally non-centrosymmetric superconductivity in multilayer systems, *J. Phys. Soc. Jpn.* **81**, 034702 (2012).
- [66] M. Sigrist, D. F. Agterberg, M. H. Fischer, J. Goryo, F. Loder, S.-H. Rhim, D. Maruyama, Y. Yanase, T. Yoshida, and S. J. Youn, Superconductors with staggered non-centrosymmetry, *J. Phys. Soc. Jpn.* **83**, 061014 (2014).
- [67] Y. Nakamura and Y. Yanase, Odd-parity superconductivity in bilayer transition metal dichalcogenides, *Phys. Rev. B Condens. Matter* **96**, 054501 (2017).
- [68] D. Möckli, Y. Yanase, and M. Sigrist, Orbitally limited pair-density-wave phase of multilayer superconductors, *Phys. Rev. B Condens. Matter* **97**, 144508 (2018).
- [69] A. Larkin and A. Varlamov, *Theory of fluctuations in superconductors*, Vol. 127 (OUP Oxford, 2005).
- [70] F. Korschelle, J. Cayssol, and A. I. Buzdin, Anomalous fluctuation regimes at FFLO transition, *EPL* **79**, 67001 (2007).
- [71] F. Korschelle, J. Cayssol, and A. I. Buzdin, Oscillations of magnetization and conductivity in anisotropic Fulde-Ferrell-Larkin-Ovchinnikov superconductors, *Phys. Rev. B Condens. Matter* **79**, 224526 (2009).
- [72] R. Wakatsuki, Y. Saito, S. Hoshino, Y. M. Itahashi, T. Ideue, M. Ezawa, Y. Iwasa, and N. Nagaosa, Nonreciprocal charge transport in noncentrosymmetric superconductors, *Sci Adv* **3**, e1602390 (2017).
- [73] R. Wakatsuki and N. Nagaosa, Nonreciprocal current in noncentrosymmetric rashba superconductors, *Phys. Rev. Lett.* **121**, 026601 (2018).
- [74] A. Daido and Y. Yanase, Rectification and nonlinear hall effect by fluctuating finite-momentum cooper pairs, *Phys. Rev. Res.* **6**, L022009 (2024).
- [75] N. Nunchot, D. Nakashima, and R. Ikeda, Fluctuation conductivity and vortex state in a superconductor with strong paramagnetic pair breaking, *Phys. Rev. B Condens. Matter* **105**, 174510 (2022).
- [76] T. Yoshida, M. Sigrist, and Y. Yanase, Complex-stripe phases induced by staggered rashba spin-orbit coupling, *Journal of the Physical Society of Japan* **82**, 074714 (2013).
- [77] See the Supplemental Material.
- [78] Y. Matsuda and H. Shimahara, Fulde-Ferrell-Larkin-Ovchinnikov state in heavy fermion superconductors, *J. Phys. Soc. Jpn.* **76**, 051005 (2007).
- [79] M. H. Fischer, M. Sigrist, D. F. Agterberg, and Y. Yanase, Superconductivity and local Inversion-Symmetry breaking, *Annu. Rev. Condens. Matter Phys.* **14**, 153 (2023).
- [80] V. Barzykin and L. P. Gor'kov, Inhomogeneous stripe phase revisited for surface superconductivity, *Phys. Rev. Lett.* **89**, 227002 (2002).
- [81] D. F. Agterberg, Novel magnetic field effects in unconventional superconductors, *Physica C Supercond.* **387**, 13 (2003).
- [82] O. V. Dimitrova and M. V. Feigel'man, Phase diagram of a surface superconductor in parallel magnetic field, *Journal of Experimental and Theoretical Physics Letters* **78**, 637 (2003).
- [83] R. P. Kaur, D. F. Agterberg, and M. Sigrist, Helical vortex phase in the noncentrosymmetric CePt3Si, *Phys. Rev. Lett.* **94**, 137002 (2005).
- [84] D. F. Agterberg and R. P. Kaur, Magnetic-field-induced helical and stripe phases in rashba superconductors, *Phys. Rev. B Condens. Matter* **75**, 064511 (2007).
- [85] O. Dimitrova and M. V. Feigel'man, Theory of a two-dimensional superconductor with broken inversion symmetry, *Phys. Rev. B Condens. Matter* **76**, 014522 (2007).
- [86] Y. Yanase and M. Sigrist, Helical superconductivity in non-centrosymmetric superconductors with dominantly spin triplet pairing, *J. Phys. Soc. Jpn.* **77**, 342 (2008).
- [87] K. V. Samokhin, Upper critical field in noncentrosymmetric superconductors, *Phys. Rev. B Condens. Matter* **78**, 224520 (2008).
- [88] K. Michaeli, A. C. Potter, and P. A. Lee, Superconducting and ferromagnetic phases in SrTiO₃/LaAlO₃ oxide interface structures: possibility of finite momentum pairing, *Phys. Rev. Lett.* **108**, 117003 (2012).
- [89] M. Houzet and J. S. Meyer, Quasiclassical theory of disordered rashba superconductors, *Phys. Rev. B Condens. Matter* **92**, 014509 (2015).
- [90] E. Bauer and M. Sigrist, *Non-centrosymmetric superconductors: introduction and overview*, Vol. 847 (Springer Science & Business Media, 2012).
- [91] N. F. Q. Yuan, Orbital fulde-ferrell-larkin-ovchinnikov state in an ising superconductor, [arXiv:2312.07053 \[cond-mat.supr-con\]](https://arxiv.org/abs/2312.07053) (2023).
- [92] Y.-M. Xie and K. T. Law, Orbital Fulde-Ferrell pairing state in moiré ising superconductors, *Phys. Rev. Lett.* **131**, 016001 (2023).
- [93] K. Nakamura, A. Daido, and Y. Yanase, Orbital effect on the intrinsic superconducting diode effect, *Phys. Rev. B Condens. Matter* **109**, 094501 (2024).
- [94] D. F. Agterberg, J. C. S. Davis, S. D. Edkins, E. Fradkin, D. J. Van Harlingen, S. A. Kivelson, P. A. Lee, L. Radzihovsky, J. M. Tranquada, and Y. Wang, The physics of Pair-Density waves: Cuprate superconductors and beyond, *Annu. Rev. Condens. Matter Phys.* **11**, 231 (2020).

Appendix A: Derivation of GL factor $\hat{\alpha}$

In this section, we demonstrate the derivation of GL factor $\hat{\alpha}$ from GL free energy,

$$F = -\frac{1}{\beta} \text{tr} \log e^{-\beta \hat{H}}. \quad (\text{A1})$$

Here, we can rewrite the Hamiltonian as

$$\hat{H} = \frac{1}{2} \sum_{\mathbf{k}} \Psi(\mathbf{k})^\dagger \hat{H}_{\text{BdG}}(\mathbf{k}) \Psi(\mathbf{k}) + 2 \sum_{\mathbf{k}} \xi(\mathbf{k}) + \sum_{m,\mathbf{k}} \frac{|\Delta|^2}{U} \quad (\text{A2})$$

with the BdG Hamiltonian \hat{H}_{BdG} ,

$$\hat{H}_{\text{N}}(\mathbf{k}) = \begin{pmatrix} H_{\text{N}}(\mathbf{k}) & 0 \\ 0 & -H_{\text{N}}(-\mathbf{k})^T \end{pmatrix}, \quad (\text{A3})$$

$$\Delta = \Delta_1 \varphi_1 + \Delta_2 \varphi_2 \quad (\text{A4})$$

$$\hat{\Delta} = \begin{pmatrix} 0 & \Delta \\ \Delta^\dagger & 0 \end{pmatrix}, \quad (\text{A5})$$

$$\hat{H}_{\text{BdG}}(\mathbf{k}) = \hat{H}_{\text{N}}(\mathbf{k}) + \hat{\Delta}, \quad (\text{A6})$$

and the Nambu spinor,

$$\Psi(\mathbf{k})^\dagger = (c_{\mathbf{k}\uparrow 1}^\dagger, c_{\mathbf{k}\downarrow 1}^\dagger, c_{\mathbf{k}\uparrow 2}^\dagger, c_{\mathbf{k}\downarrow 2}^\dagger, c_{-\mathbf{k},\uparrow 1}, c_{-\mathbf{k},\downarrow 1}, c_{-\mathbf{k},\uparrow 2}, c_{-\mathbf{k},\downarrow 2}). \quad (\text{A7})$$

Then, the GL free energy is

$$F = -\frac{1}{2\beta} \sum_{\mathbf{k}} \text{tr} \log \left(1 + e^{-\beta E_{\text{N}}(\mathbf{k})} \right) + 2 \sum_{\mathbf{k}} \xi(\mathbf{k}) + \sum_{m,\mathbf{k}} \frac{|\Delta|^2}{U} \quad (\text{A8})$$

$$= F|_{\Delta=0} + \delta F, \quad (\text{A9})$$

where $E_{\text{N}}(\mathbf{k})$ represents eigenvalues of $\hat{H}_{\text{BdG}}(\mathbf{k})$. By expanding δF by Δ , we can obtain the GL factor $\hat{\alpha}$,

$$\begin{aligned} \delta F/V &= \sum_m \frac{|\Delta|^2}{U} + \frac{1}{2\beta V} \sum_{\mathbf{k}, \omega_n} \text{tr}_{\text{N}} \left(\frac{1}{i\omega_n - H_{\text{N}}(\mathbf{k})} \Delta(\mathbf{k}) \frac{1}{i\omega_n + H_{\text{N}}(-\mathbf{k})^T} \Delta(\mathbf{k})^\dagger \right) + \mathcal{O}(\Delta^4) \\ &= \sum_m \frac{|\Delta_m|^2}{U} + \frac{1}{2V} \sum_{\mathbf{k}, n, m} F_{nm}(\mathbf{k}) \left[\Delta_1^* \Delta_1 |\langle u_n(\mathbf{k}) | \varphi_1 | u_m^*(-\mathbf{k}) \rangle|^2 + \Delta_2^* \Delta_2 |\langle u_n(\mathbf{k}) | \varphi_2 | u_m^*(-\mathbf{k}) \rangle|^2 \right. \\ &\quad \left. + \Delta_1^* \Delta_2 \langle u_m^*(-\mathbf{k}) | \varphi_1^\dagger | u_n(\mathbf{k}) \rangle \langle u_n(\mathbf{k}) | \varphi_2 | u_m^*(-\mathbf{k}) \rangle + \Delta_2^* \Delta_1 \langle u_m^*(-\mathbf{k}) | \varphi_2^\dagger | u_n(\mathbf{k}) \rangle \langle u_n(\mathbf{k}) | \varphi_1 | u_m^*(-\mathbf{k}) \rangle \right] + \mathcal{O}(\Delta^4) \\ &= (\Delta_1^* \ \Delta_2^*) \hat{\alpha} \begin{pmatrix} \Delta_1 \\ \Delta_2 \end{pmatrix} + \mathcal{O}(\Delta^4) \end{aligned} \quad (\text{A10})$$

with $F_{mn}(\mathbf{k})$ in Eq. (12). Then we obtain the expression of $\hat{\alpha}$ given in Eq. (11).

We prove that $\sigma_{\text{BCS-PDW}}$ vanishes in the system in the perpendicular magnetic field. In this case, the system has both C_{2z} symmetry and M_z symmetry,

$$\hat{\alpha}(\mathbf{q}) = \hat{\alpha}(-\mathbf{q}), \quad (\text{A11})$$

$$\sigma_x \hat{\alpha}(\mathbf{q}) \sigma_x^\dagger = \hat{\alpha}(\mathbf{q}). \quad (\text{A12})$$

Thus, we can express $\hat{\alpha}(\mathbf{q})$ by,

$$\hat{\alpha}(\mathbf{q}) = \begin{pmatrix} a(\mathbf{q}) & b(\mathbf{q}) \\ b(\mathbf{q}) & a(\mathbf{q}) \end{pmatrix}, \quad (\text{A13})$$

with real numbers $a(\mathbf{q})$ and $b(\mathbf{q})$. Accordingly, eigenvec-

tors of $\hat{\alpha}$ are given by

$$|\text{BCS}\rangle = \frac{1}{\sqrt{2}} \begin{pmatrix} 1 \\ 1 \end{pmatrix}, \quad (\text{A14})$$

$$|\text{PDW}\rangle = \frac{1}{\sqrt{2}} \begin{pmatrix} 1 \\ -1 \end{pmatrix}, \quad (\text{A15})$$

regardless of \mathbf{q} . This forces $\sigma_{\text{BCS-PDW}}$ to vanish, since

$$\begin{aligned} \langle \text{BCS} | j_i | \text{PDW} \rangle &= \frac{1}{2} (1 \ 1) \partial_i \begin{pmatrix} a(\mathbf{q}) & b(\mathbf{q}) \\ b(\mathbf{q}) & a(\mathbf{q}) \end{pmatrix} \begin{pmatrix} 1 \\ -1 \end{pmatrix} \\ &= \frac{1}{2} \partial_i (a(\mathbf{q}) + b(\mathbf{q}) - a(\mathbf{q}) - b(\mathbf{q})) \\ &= 0. \end{aligned} \quad (\text{A16})$$

Thus, the linear paraconductivity is given by summing up the BCS and PDW contributions, σ_{BCS} and σ_{PDW} , in the system in the perpendicular magnetic field.